ORIGINAL ARTICLE

A smart O_2-generating nanocarrier optimizes drug transportation comprehensively for chemotherapy improving

Xiaojuan Zhang[a,†], Chuanchuan He[a,†], Yun Sun[b], Xiaoguang Liu[a], Yan Chen[a], Chen Chen[a], Ruicong Yan[a], Ting Fan[a], Tan Yang[a], Yao Lu[a], Jun Luo[a,*], Xiang Ma[a,*], Guangya Xiang[a,*]

[a]School of Pharmacy, Tongji Medical College, Huazhong University of Science and Technology, Wuhan 430030, China
[b]Institute of Traditional Chinese Medicine, Xinjiang Medical University, Urumqi 830011, China

Abstract Drug transportation is impeded by various barriers in the hypoxic solid tumor, resulting in compromised anticancer efficacy. Herein, a solid lipid monostearin (MS)-coated CaO_2/MnO_2 nanocarrier was designed to optimize doxorubicin (DOX) transportation comprehensively for chemotherapy enhancement. The MS shell of nanoparticles could be destroyed selectively by highly-expressed lipase within cancer cells, exposing water-sensitive cores to release DOX and produce O_2. After the cancer cell death, the core-exposed nanoparticles could be further liberated and continue to react with water in the tumor extracellular matrix (ECM) and thoroughly release O_2 and DOX, which exhibited cytotoxicity to neighboring cells. Small DOX molecules could readily diffuse through ECM, in which the collagen deposition was decreased by O_2-mediated hypoxia-inducible factor-1 inhibition, leading to synergistically improved drug penetration. Concurrently, DOX-efflux-associated P-glycoprotein was also inhibited by O_2, prolonging drug retention in cancer cells. Overall, the DOX transporting processes from nanoparticles to deep

tumor cells including drug release, penetration, and retention were optimized comprehensively, which significantly boosted antitumor benefits.
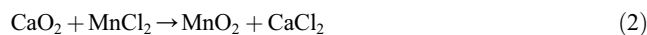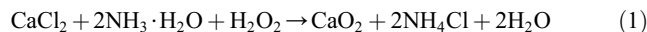
1. Introduction

Despite the rapid development of innovative cancer therapeutic strategies such as photodynamic therapy (PDT), radiotherapy, and immunotherapy, chemotherapy is still the most common-used treatment in the clinic[1]. Unfortunately, due to nonselective drug distribution and poor pharmacokinetics, the administration of free drugs always results in unsatisfactory therapeutic outcomes and severe systemic cytotoxicity[2]. With the advent of nanotechnology, nanoscale drugs were developed to optimize drug pharmacokinetics[3]. However, it is a great challenge to realize the good performance of nanomedicine concurrently in the systemic circulation and inside the tumor[4]. For example, nanoparticle (NP) enables drug benefits of avoiding excretion and passive accumulation in solid tumor regions by the enhanced permeability and retention (EPR) effect but meanwhile impedes drug penetration through the extracellular matrix (ECM)[5]. In addition, negatively charged NPs undergo stable circulation in blood vessels and show safety to normal tissues, whereas positive charged ones behave better in cellular uptake in tumor tissues[6]. To reconcile these contrary requirements in one design, the strategy that constructing smart nanomedicine with tumor-responsive convertible capacity had been proposed to significantly elevate intratumoral activities of nanomedicines[7].

Apart from the NP properties, unfavorable factors of tumor microenvironment (TME) also contribute to poor therapeutic outcomes[8]. Hypoxia, one of the most characteristic hallmarks of TME, was proved to play a crucial role in tumor progress and therapeutic resistance[9]. It has been reported that hypoxia upregulates hypoxia-inducible factor 1α (HIF-1α) and P-glycoprotein (P-gp), which mediates drug efflux and reduced chemotherapy[10]. As one of the main components in ECM, collagen is also expressed in an HIF-1 dependent manner[11]. Under hypoxic conditions, collagen deposition increases the density of ECM, which impedes the penetration of drugs and nanodrugs. In recent years, considerable efforts have been devoted to modulate the factors of TME and enhance therapeutic efficacy through various mechanisms. Particularly hypoxia, which regulates multiple genes and proteins, has been demonstrated to be an effective target for enhancing different therapeutic modalities including chemotherapy[12], PDT[13] and immunotherapy[14].

Conceivably, smart NPs with both tumor-responsive size-convertible capacity and TME-modulation ability may realize synergistic effects in bolstering nanomedicine antitumor efficacy[15,16]. Recently, Cui et al.[17] established a hyaluronidase (HAase)-modified ZnO NP to improve doxorubicin (DOX) chemotherapy. Hyaluronic acid (HA) is another main component of ECM that could be degraded by HAase to enhance nanodrug diffusion[18]. Through the pH-responsive size reduction of ZnO NPs and release of HAase, deep tumor penetration was realized due to the synergism of the neighboring effect and HAase-mediated HA

degradation. However, in addition to tumor penetration, such NPs still face obstacles that reduce chemotherapy. First, most internal-stimulants (for example, H^+ and glutathione) could be consumed in ZnO disintegration[19], and thus the NPs might not able to realize sufficient drug release in TME. Second, the intracellular DOX could be pumped out from hypoxic cells by P-gp[20]. Hence, to further promote drug bioavailability and increase its anti-tumor effects, it is highly desirable to optimize drug transportation comprehensively (*i.e.*, not only drug penetration but also sufficient drug release and drug retention) by constructing switchable NPs that can respond to an infinite stimulus (such as water) and modulate multi-targeted TME factors (such as hypoxia).

Herein, we designed an O_2-generating CaO_2/MnO_2 nanocarrier to improve DOX transportation comprehensively and finally enhance chemotherapy. As shown in Scheme 1A, the DOX molecules were preloaded in CaO_2 matrix by chelating with Ca^{2+} during the synthesis of CaO_2 according to Eq. (1). After the addition of $MnCl_2$, MnO_2 was formed *in situ* on CaO_2 surface according to Eq. (2). The obtained drug-loaded cores were then stabilized by a solid lipid monostearin (MS) and PEG-lipids, which could prevent potential drug leakage during the circulatory process and enable tumor lipase responsiveness of NPs[21].

$$CaCl_2 + 2NH_3 \cdot H_2O + H_2O_2 \rightarrow CaO_2 + 2NH_4Cl + 2H_2O \quad (1)$$

$$CaO_2 + MnCl_2 \rightarrow MnO_2 + CaCl_2 \quad (2)$$

The anticancer mechanisms were proposed as following: (1) by EPR effects, the NPs passively accumulated in tumor sites and were taken up by tumor cells[22]; (2) the highly-expressed lipase in cancer cells disintegrated the MS layers of NPs and uncovered the active drug-loaded cores; (3) the exposed DOX-CaO_2/MnO_2 cores reacted with water according to Eqs. (3) and (4), leading to the burst release of DOX and O_2; (4) O_2-mediated HIF-1/P-gp inhibition prolonged DOX retention in cancer cells for severer cell death; (5) The dead cells liberated core-exposed NPs, which continued to sufficiently release DOX and O_2 molecules in the ubiquitous aqueous environment of ECM; (6) The molecular DOX could readily diffuse through ECM, and O_2 synergistically improved drug penetration by decreasing the collagen deposition of ECM through HIF-1α degradation; (7) DOX and O_2 reached to the deep tumor region and induced cell death as the step 4.

$$CaO_2 + 2H_2O \rightarrow H_2O_2 + Ca(OH)_2 \quad (3)$$

$$2H_2O_2 (MnO_2) \rightarrow 2H_2O + O_2 \uparrow \quad (4)$$
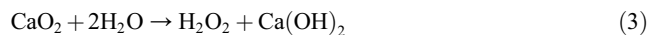
Apart from a drug delivery vehicle, CaO_2 acted as the template and reactant of MnO_2 synthesis, which greatly augmented the O_2-producing efficiency of NPs. Through the rational design and construction of this smart/TME-modulated nanocarrier, sufficient drug release, synergistic drug penetration, and prolonged drug
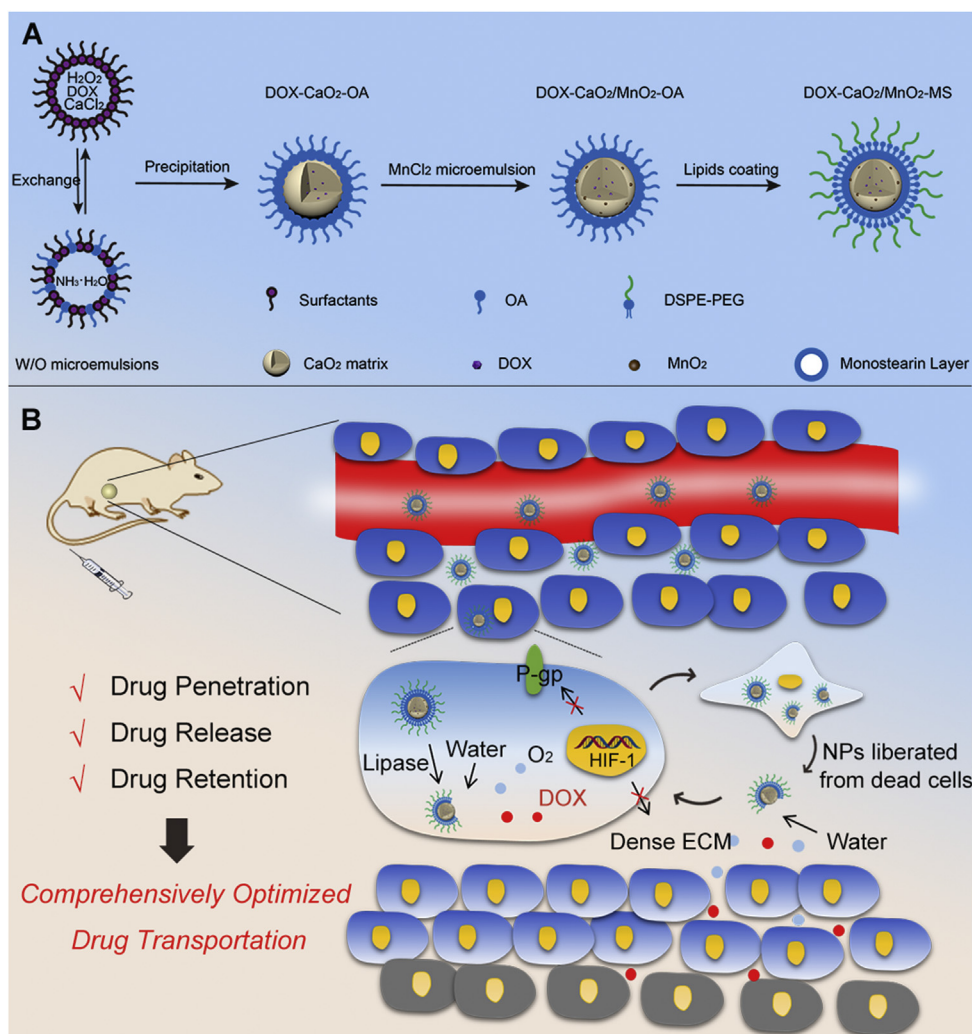
Scheme 1   (A) Synthetic procedure of DOX-CaO$_2$/MnO$_2$-MS NPs; (B) Schematic diagram of DOX-CaO$_2$/MnO$_2$-MS NPs for comprehensively optimized drug transportation.

retention were concurrently realized, contributing to comprehensive optimization of drug transportation from NPs to deep tumor cells and finally improvement of chemotherapy. We envision that such solid lipid-coated CaO$_2$/MnO$_2$ nanocarriers also hold great potential in other O$_2$-dependent cancer therapeutic modalities such as PDT, radiation therapy, and immunotherapy.

2.   Materials and methods

2.1.   Materials

All reagents and solvents were purchased commercially and used without further purification unless specially noted. The deionized water used in all experiments was produced by a Milli-Q water purification system with a specific resistance greater than 18.25 MΩ cm at 25 °C. Doxorubicin hydrochloride was supplied by Dalian Meilun Biotech Co., Ltd. (Dalian, China). Fetal bovine serum (FBS) was purchased from Zhejiang Tianhang Biological Technology Co., Ltd. (Hangzhou, China). 3-(4,5-Dimethylthiazol-2-yl)-2,5-diphenyltetrazolium bromide (MTT) was purchased from Sigma (St. Louis, MO, USA). 1,2-Distearoyl-*sn*-glycero-3-

phosphoethanolamine-*N*-[methoxy(polyethylene glycol)-2000] (DSPE-PEG2000) was obtained from A.V.T. Pharmaceutical Co., Ltd. (Shanghai, China). H$_2$O$_2$ assay kit was purchased from Solarbio (Beijing, China). Monostearin was obtained from Aladdin Reagents Co., Ltd. Other chemicals were purchased from Sigma−Aldrich Chemical Co. (St. Louis, USA).

2.2.   Animals model

BALB/c nude mice (female, 4−5 weeks old) were obtained from Beijing Huafukang Bioscience Technology Co., Ltd. (Beijing, China). The mice were kept in filter-topped cages with standard rodent chow, all with food and water available ad libitum, and with a 12 h light/dark cycle. The experimental protocol was approved by Committee on Ethical Animal Experiment at Huazhong University of Science and Technology, Wuhan, China.

2.3.   Cell line and culture

SKOV3 (human ovarian carcinoma) cells were obtained from Procell Life Science & Technology Co., Ltd. (Wuhan, China), L02

(human hepatocytes) cell line was obtained from KeyGEN biotechnology Co., Ltd. (Nanjing, China). Cells were cultured in Dulbecco's modified Eagle's medium (DMEM) with 10% FBS, 100 U/mL penicillin, and 100 μg/mL streptomycin. The device for hypoxic cell incubation was purchased from PUHE Biotechnology Co., Ltd. (Wuxi, China), which could construct a hypoxic and humid atmosphere at 37 °C in 5% CO_2 and 1% O_2.

2.4. Preparation of NPs

A 10-mL mixture of cyclohexane/Igepal CO-520 (71:29, v/v) consisting of 500 μL of ammonium hydroxide and 60 μL of oleic acid (OA) was stirred vigorously at room temperature. Another 10-mL mixture of cyclohexane/Igepal CO-520 (71:29, v/v) consisting of 250 μL of hydrogen peroxide, 250 μL of aqueous calcium chloride (4 mol/L) and 5 mg of DOX was stirred similarly. The two microemulsions were stirred continuously for 10 min. Afterward, both microemulsions were mixed, followed by an additional 30 min's stirring. To obtain DOX-CaO_2-OA NPs, 15 mL of ethanol was used to destroy the microemulsion and precipitate the NPs, which were further re-dispersed in 15 mL cyclohexane. To introduce MnO_2, 1 mL of microemulsion containing 50 μL of $MnCl_2$ solution (1 mol/L) was added to above DOX-CaO_2-OA NPs. After the reaction for 5 min, the brownish product was collected by ethanol precipitation and centrifugation. The obtained DOX-CaO_2/MnO_2-OA NPs were stored in $CHCl_3$.

For further use, 300 μL of MS and 300 μL of DSPE-PEG2000 (10 mmol/L) in chloroform were added to the above DOX-CaO_2/MnO_2-OA NPs solution. After rotary evaporation, a thin film was formed, followed by the addition of 3 mL of distilled water. The final DOX-CaO_2/MnO_2-MS NPs were obtained by sonification for 20 s.

2.5. Characterization of NPs

The shapes and crystalline structures of NPs were characterized using microscopic and spectroscopic methods. Briefly, a drop of the sample dispersion was placed onto a copper grid and observed by transmission electron microscopy (TEM) after evaporation of the solvent at room temperature. The graphs were obtained on a Tecnai (G2 20, FEI Co., Netherlands) at an acceleration voltage of 200 kV. Furthermore, the X-ray photoelectron spectroscopy (XPS) samples were lyophilized, and the XPS patterns were operated on an Axis-ultra Dld-600 W (Kratos, Japan) photoelectron spectrometer. Powder X-ray diffraction (XRD) patterns were collected on a Rigaku RINT-2200 diffractometer with Cu Kα radiation (40 kV, 30 mA) from 5° to 90° in 0.013° steps at a scan speed of 1° (2θ)/min. UV-Vis spectrometer was used to measure the absorption from 350 nm to 750 nm of the NPs solutions in a quartz cell. The hydrodynamic size and zeta potential of NPs were obtained by Dynamic Light Scattering (DLS) measurement.

2.6. Quantitative analysis

CaO_2 was quantified by a commercial H_2O_2 Assay Kit based on its H_2O_2 production capability. In brief, 25 μL of DOX-CaO_2/MnO_2-MS solution was added to 225 μL of acetone. Then 25 μL of acidic $Ti(SO_4)_2$ solution and 50 μL of ammonium hydroxide were added to the above solution, followed by centrifugation for 10 min (4000×g). The supernatant was abandoned and the resulted precipitate was dissolved in H_2SO_4 solution (1 mol/L).

The absorbance of the final solution at 415 nm was measured by UV-Vis spectroscopy. DOX contents in DOX-CaO_2/MnO_2-MS were also measured using UV-Vis spectroscopy. The amount of Mn was detected by inductively coupled plasma atomic absorption spectrometry (ICP-AAS).

2.7. Cellular uptake

The red fluorescence of DOX was employed to track the intracellular locations of DOX. Briefly, cells were seeded into the 12-well plate (NEST, Wuxi, China) at a density of 2×10^5 per well. After 24 h, the cells were exposed to free DOX and DOX-CaO_2/MnO_2-MS NPs (DOX concentration: 1 μmol/L), respectively. After incubation for different periods, the initial medium was removed and the cells were washed with phosphate-buffered saline (PBS) three times. Finally, the cells were counterstained with 4′,6-diamidino-2-phenylindole (DAPI: 1.2 μg/mL) for 8 min and then rinsed with PBS. The cells were imaged with a fluorescence microscope (Zeiss LSM 510).

2.8. Cytotoxic activities

By measuring the ability of live cells to transform MTT to a purple formazan dye, the cell viability after NPs treatment was determined. Firstly, cells were seeded in 96-well tissue culture plates overnight at a density of 4×10^3 cells per well. Then the cells were incubated with different concentrations of drugs for 24 h. After that, the medium was aspirated, and 20 μL/well of MTT solution (5 mg/mL in PBS) was added. Four hours later, the supernatants were removed carefully, followed by the addition of 150 μL/well of dimethyl sulfoxide. The color intensity of the formazan solution, which reflects the cell growth condition, was measured at 570 nm using a microplate spectrophotometer (VersaMax, USA). All complexes doses were parallel tested in quintuplicate, and the data were presented as averages of three independent experimental standard deviations (SD).

For apoptosis analysis, SKOV3 cells were seeded on 6-well plates and cultured in DMEM with 10% FBS for 12 h. Then the medium was replaced with fresh DMEM with 10% FBS, and different NPs groups were added (DOX concentration: 1 μmol/L). The cells were collected and stained with an Annexin V-FITC Apoptosis Detection Kit (KeyGen Biotech). A BD Accuri C6 Flow Cytometer was used for analysis.

2.9. Neighboring effect

SKOV3 cells seeded on 24 well plates (Corning, USA, 5×10^5/well and allowed to grow overnight) with coverslips were pretreated with the free DOX, DOX-$CaCO_3$-MS, and DOX-CaO_2/MnO_2-MS NPs at DOX concentration of 10 μg/mL for 8 h. The pretreated cells (a) were washed with PBS and then co-incubated with the fresh cells on a coverslip (b) for 24 h in a fresh culture medium. Then, (b) was withdrawn and co-incubated with the fresh cells on another new coverslip (c) for 24 h in a fresh culture medium. The cells (a, b and c) were then washed by ice-cold PBS thrice, stained with Hoechst 33,342, and observed using confocal laser scanning microscopy (CLSM).

Apoptosis assay was also conducted to verify the neighboring effect. SKOV3 cells were seeded in 6-well plates at the cell density of 1×10^6/well overnight 20 h. Then the cells were

incubated with free DOX, DOX-CaCO$_3$-MS or DOX-CaO$_2$/MnO$_2$-MS NPs at 37 °C for 8 h, in which the DOX concentrations were 4 µg/mL. Afterward, the cells were washed with PBS, trypsinized and mixed with blank cells at the ratio of 1:10, followed by cultivation in 20-mm glass-bottom culture dishes for 24 h. After that, Hoechst 33,342 and Annexin V-FITC were used to stain the cells according to manufacturer's protocol. Samples were observed under CLSM.

2.10. Intracellular O$_2$ determination

Intracellular O$_2$ levels were determined using an optical probe, [Ru (dpp)$_3$]Cl$_2$. First, SKOV3 and L02 cells were incubated under hypoxic conditions for 24 h, after which [Ru (dpp)$_3$]Cl$_2$ (10 µg/mL) was added for another 12 h incubation. Then the cells were treated with NPs for 2 h. After that, the cells were washed with PBS twice, and the intracellular O$_2$ levels were measured using a fluorescence microscope by detecting the fluorescence of [Ru (dpp)$_3$]Cl$_2$ (λ_{ex} = 450 nm, λ_{em} = 610 nm).

2.11. Western blot analysis

Following the treatments with different drugs, total cellular proteins were obtained using RIPA buffer (Applygen Technologies, Inc., Beijing, China). Protein (30 µg) was added per lane and proteins were separated by SDS-PAGE on 10% gel and transferred onto a polyvinylidene difluoride (PVDF) membrane. Following blocking with 5% skimmed milk at room temperature for 1 h, the membranes were sequentially incubated with primary antibodies overnight at 4 °C. The membrane was washed with TBST (PBS with 0.1% Tween-20) 3 times and then incubated with HRP-conjugated goat (polyclonal) anti-rabbit/anti-mouse IgG secondary antibody for 1 h at room temperature. Then the membrane was washed another 4 times and observed in an enhanced chemiluminescence system (PerkinElmer, Waltham, MA, USA). β-Tubulin was used as a loading control. Antibodies used for western blotting included those against HIF-1α (1:1000, Cell Signaling), P-gp (1:1000, Cell Signaling), connective tissue growth factor (CTGF, 1:1000, Cell Signaling), and Collagen I (1:1000, Cell Signaling).

2.12. Drug penetration and inhibition in multicellular tumor spheroids (MCTS)

The formation of MCTS was monitored using an optical microscope (TE2000-S, Nikon, Japan). The tumor spheroids with diameters of about 400 µm were incubated with the free DOX, DOX-CaCO$_3$-MS, DOX-CaO$_2$-MS, and DOX-CaO$_2$/MnO$_2$-MS NPs at the DOX concentration of 2 µmol/L for 24 h, respectively. Then, the tumor spheroids were washed thrice with ice-cold PBS, fixed with paraformaldehyde for 30 min, and placed in cavity microscope slides. The images of the tumor spheroids were acquired using Z-stack imaging with 20 µm intervals from the top of the spheroid to the middle by CLSM. For the MCTS inhibition, the tumor spheroids with diameters of about 200 µm were divided into groups (n = 5). The selected spheroids were treated with saline, free DOX, DOX-CaCO$_3$-MS, DOX-CaO$_2$-MS, and DOX-CaO$_2$/MnO$_2$-MS NPs. The spheroids were allowed to incubate at 37 °C for 9 days. The diameter of the spheroids was imaged and recorded every 2 days using an optical microscope.

2.13. In vivo imaging and antitumor study

The in vivo imaging study was conducted on SKOV3 cells bearing mice by a noninvasive optical imaging system (Pearl Trilogy, LI-COR, USA). The hydrophobic fluorescein DiR was loaded into the CaO$_2$/MnO$_2$-MS by a film dispersion method to produce CaO$_2$/MnO$_2$-DiR/MS NPs. BALB/c nude mice were intravenously injected with CaO$_2$/MnO$_2$-DiR/MS NPs or free DiR at the dosage of 5 µg DiR per mice. At 0.5, 4, 8, 24, and 48 h, the fluorescence intensity images of each mouse were captured.

The SKOV3 bearing nude mice were randomly divided into four groups (n = 5) to study the in vivo antitumor efficacy of NPs. On Days 7, 10, 13 and 16 after tumor inoculation, the mice were injected via the tail vein with saline, free DOX, CaO$_2$/MnO$_2$-MS, and DOX-CaO$_2$/MnO$_2$-MS NPs at 5 mg/kg of DOX or its equivalent. Tumor sizes and animal body weights were monitored every two days after treatment. On Day 24, the mice were sacrificed, major organs and tumor tissues were acquired for further analysis.

2.14. Statistical analysis

All data were taken from three independent experiments and then expressed as means $\pm$ standard deviation (SD). One-way ANOVA was performed to compare the statistical analysis by GraphPad Prism 5.0 (San Diego, CA, USA).

3. Results and discussion

3.1. Preparation and characterization

According to our previous work, CaO$_2$ NPs were synthesized by the reaction of CaCl$_2$, H$_2$O$_2$, and NH$_3$·H$_2$O in reverse microemulsions[23]. To prepare drug-preloaded CaO$_2$ NPs with a hydrophobic coating, DOX and OA were introduced into the microemulsion system. Through the alkaline NH$_3$·H$_2$O-facilitated deprotonation, DOX chelated with Ca^{2+} to form the Ca−DOX complex and was finally entrapped in CaO$_2$ matrix[24]. Similarly, the deprotonated carboxyl groups of OA molecules also coordinated with Ca^{2+}, enabling the hydrophobic surface coating of NPs by long-chain alkyl[25]. As shown in Fig. 1A, the purple product DOX-CaO$_2$-OA showed remarkable solubility in non-polar solutions such as CHCl$_3$. From the image obtained by TEM, we found that the NP size was about 50 nm with irregular morphology.

To synthesize MnO$_2$-doped NPs, the obtained DOX-CaO$_2$-OA NPs were re-dispersed in cyclohexane, followed by adding a small volume of MnCl$_2$-contained microemulsion. Due to the hydrophilic property of the interface between CaO$_2$ and OA, the aqueous MnCl$_2$ could easily diffuse into their interlayer and react with CaO$_2$. After that, the solution color turned from purple to brownish due to the formation of MnO$_2$ (denoted as DOX-CaO$_2$/MnO$_2$-OA). To the best of our knowledge, this trial may be the first to synthesize MnO$_2$ NPs by a metal peroxide. Similar to DOX-CaO$_2$-OA observed by TEM, the DOX-CaO$_2$/MnO$_2$-OA NPs were well-dispersed in CHCl$_3$ with a diameter of approximately 50 nm (Fig. 1B).

The DOX-CaO$_2$/MnO$_2$-OA NPs were further surface-modified with 1,2-distearoyl-sn-glycero-3-phosphoethanolamine-N-[amino (polyethylene glycol)-2000] (DSPE-PEG2000) and MS to construct the hydrophilic DOX-CaO$_2$/MnO$_2$-MS NPs. As can be seen in Fig. 1C, after coating with lipids, the particle sizes became
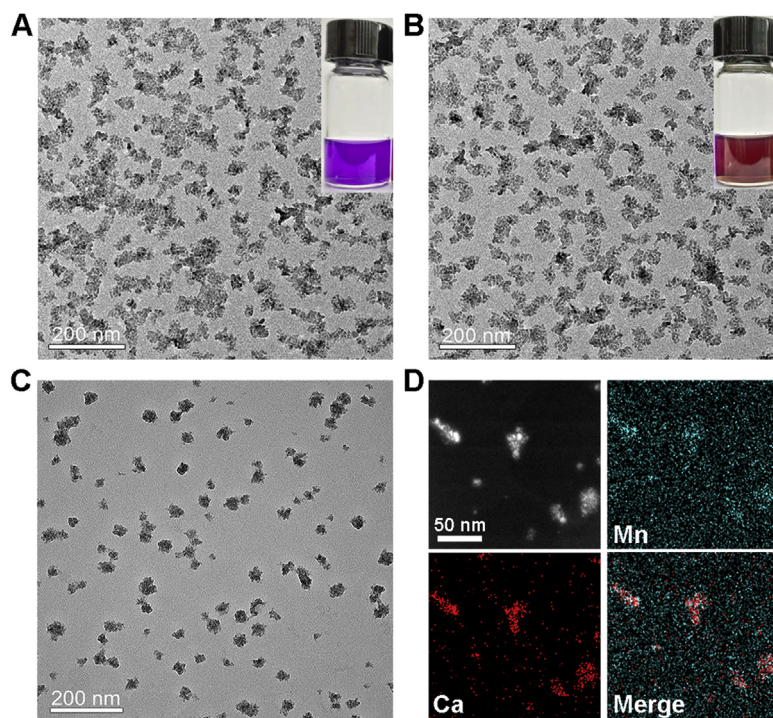
Figure 1 (A) TEM image of DOX-CaO$_2$-OA NPs, scale bar = 200 nm. Insert: photograph of DOX-CaO$_2$-OA NPs dissolved in CHCl$_3$. (B) TEM image of DOX-CaO$_2$/MnO$_2$-OA NPs, scale bar = 200 nm. Insert: photograph of DOX-CaO$_2$/MnO$_2$-OA NPs dissolved in CHCl$_3$. (C) TEM image of DOX-CaO$_2$/MnO$_2$-MS NPs, scale bar = 200 nm. (D) Elemental mapping of DOX-CaO$_2$/MnO$_2$-MS NPs, scale bar = 50 nm.

slightly larger (about 60 nm). The hydrodynamic size of DOX-CaO$_2$/MnO$_2$-MS NPs was measured to be 217.7 nm by DLS (Supporting Information Fig. S1), sharply larger than the results obtained by TEM. This could be explained by the existence of PEG2000 and the hydration shell of NPs. In addition, the zeta potential of NPs was determined (−10.8 mV), which proved the MS-coating of NPs. The elemental mapping images recorded in Fig. 1D demonstrate the existence of Ca, Mn, indicating the formation of CaO$_2$/MnO$_2$ nano-complex.

Further qualitative analysis was conducted using XRD and XPS. As shown in Fig. 2A, Mn signal was detected in the XPS spectrum of DOX-CaO$_2$/MnO$_2$-OA NPs, proving the synthesis of MnO$_2$. Besides, XPS deconvoluted spectra for O1s orbital[26] showed both the signals of O$^{2−}$ and O$^−$, demonstrating the existence of CaO$_2$/MnO$_2$ (Fig. 2B). In XRD results (Fig. 2C), CaO$_2$ representing specific peaks (2θ = 30.1°, 35.6°, 47.3°) were observed in both spectra of CaO$_2$-OA and CaO$_2$/MnO$_2$-OA NPs, which indicated the maintenance of crystal structure of CaO$_2$ matrix after the MnO$_2$ introduction[27]. Overall, these results confirmed that CaO$_2$/MnO$_2$ nanocomposites were successfully synthesized in reverse microemulsions.

According to the previous research, the formation of the Ca−DOX complex leads to the red-shift of its UV-Vis absorption peak from 480 to 550 and 590 nm[28]. As shown in Fig. 2D, the peaks at around 550 and 590 nm were detected in DOX-CaO$_2$/MnO$_2$-MS NPs, indicating that DOX was loaded in the CaO$_2$ matrix by Ca-DOX coordination. Interestingly, the peak at 480 nm was recovered after NPs incubating with lipase and HCl, which inferred that the encapsulation of DOX by MS-coated CaO$_2$/MnO$_2$ nanocarrier did not impact its structure. UV-Vis spectrophotometry was also applied to determine the loading content of DOX in

DOX-CaO$_2$/MnO$_2$-MS NPs, which was calculated to be 5.5% (w/w). The inorganic skeleton CaO$_2$ [38.4% (w/w)] was quantified by Ti(SO$_4$)$_2$ solution with the aid of UV-Vis spectrophotometry, and MnO$_2$ [2.9% (w/w)] was measured by inductively coupled plasma atomic absorption spectrometry (ICP-AAS).

3.2. Stability and drug release

To evaluate the applicability of the DOX-CaO$_2$/MnO$_2$-MS NPs as a nanomedicine, the stability of NPs was first assessed in simulated physiological conditions. As shown in Fig. 3A, the average sizes of the DOX-CaO$_2$/MnO$_2$-MS NPs remained nearly unchanged at the range of 200−250 nm after incubation in saline, PBS, and FBS for one week, indicating the good stability of MS-based NPs under physiological conditions.

In contrast to normal cells, tumor cells express a higher level of lipase for signaling and metabolic demands, which can catalyze the hydrolysis of solid lipids[29]. Accordingly, the solid lipid MS-coated NPs were expected to respond to lipase and release drugs in a lipase-dependent manner. To validate this assumption, we first tested the drug release profile of NPs in solutions. As exhibited in Fig. 3B, DOX from DOX-CaO$_2$/MnO$_2$ NPs released completely due to the water-sensitiveness of CaO$_2$ and the lack of MS coating. However, DOX-CaO$_2$/MnO$_2$-MS NPs showed significantly slow drug release property with merely 15% of DOX being released in lipase-free solution. This could well-demonstrate the protection of CaO$_2$/MnO$_2$ and drug preserving ability by MS shell which guaranteed the stability of NPs during blood circulation. After NPs incubating with lipase for 48 h, the loaded DOX was totally released. It is worth mentioning that the well-explored pH-responsive nanocarriers might not be able to efficiently unload the
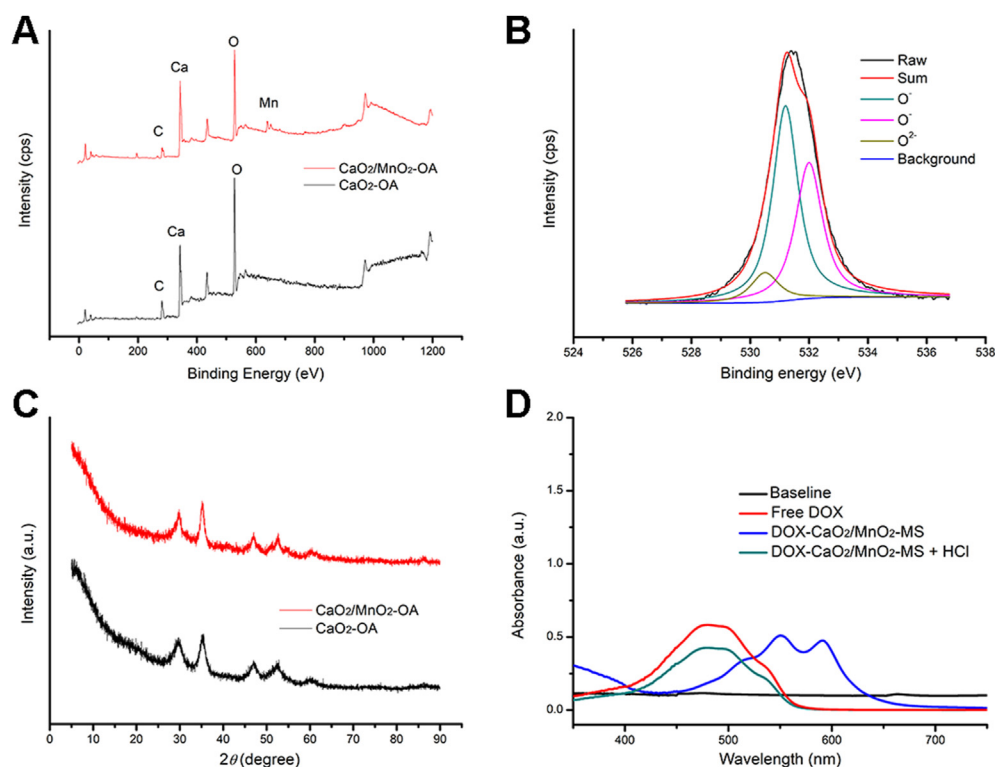
Figure 2 (A) XPS spectra of CaO_2-OA and CaO_2/MnO_2-OA NPs. (B) XPS deconvoluted spectra for O_{1s} orbital for CaO_2/MnO_2-OA NPs. (C) XRD spectra of CaO_2-OA and CaO_2/MnO_2-OA NPs. (D) UV−Vis spectra of free DOX, DOX-CaO_2/MnO_2-MS, and DOX-CaO_2/MnO_2-MS + HCl.

drugs due to the consumption of H^+. However, these lipase-triggered water-responsive NPs could achieve efficient drug release due to the existence of a ubiquitous aqueous environment in cells. Besides, the thorough decomposition of CaO_2 enabled the high biodegradability of NPs with less inorganic compounds retention in tissues, which enabled their biosafety[30].

Furthermore, the O_2-generating capacity of NPs was also investigated in solutions containing lipase. First, we confirmed that CaO_2 could react with water to produce a large amount of H_2O_2 (Fig. 3C). After the introduction of MnO_2, the generated H_2O_2 was decomposed into O_2, leading to a less level of H_2O_2. As can be seen in Fig. 3D, minimal O_2 was detected in DOX-CaO_2/MnO_2-MS NPs solution without lipase, further demonstrating their stability. Whereas in the presence of lipase, abundant O_2 was generated by DOX-CaO_2/MnO_2-MS NPs after 3 h, which proved the lipase-triggered O_2 generation ability of NPs. In the group of DOX-CaO_2-MS NPs, the lack of MnO_2 enabled the NPs with compromised O_2 generating ability. Collectively, these results inferred that DOX-CaO_2/MnO_2-MS NPs could keep stable in physiological conditions and selectively responded to the environment with a high level of lipase to efficiently release drug and O_2.

3.3. Cellular uptake

SKOV3 human ovarian cancer cells and L02 human hepatocytes cells were chosen to explore the *in vitro* cellular uptake profile of DOX-CaO_2/MnO_2-MS NPs. The fluorescence of DOX was detected to trace the drug molecules with the assistance of CLSM. As depicted in Supporting Information Fig. S2A and Fig. 4A, the DOX signal was only detected in

the cytoplasm of NPs-treated cells in early periods (0.5, 1, and 2 h), until 4 h it displayed in the nuclei. However, free DOX entered the nuclei of SKOV3 cells after incubation for merely 0.5 h (Supporting Information Fig. S2B). It might because that the endocytosis and drug release processes of NPs are the prerequisite of DOX entering the nuclei, but free DOX can diffuse into nuclei without these processes. Nevertheless, NPs-incubated L02 cells did not exhibit significant DOX fluorescence in the nuclei (Fig. 4B), indicating that the drug release of DOX-CaO_2/MnO_2-MS NPs was not sufficiently triggered due to the lower lipase activity of L02 cells. As a consequence, DOX molecules could not be liberated from NPs and enter the nuclei, which might contribute to less toxicity to normal tissues. These results demonstrated that these MS-based NPs exhibited cancer cell-selective drug release and thereby satisfactory biosafety to normal cells.

3.4. Enhanced anticancer efficacy in vitro

Furthermore, the anticancer efficacy of the NPs *in vitro* was evaluated against SKOV3 and L02 cells by MTT assay. As expected, the cytotoxicity of free DOX towards hypoxic cells was lower than that in normoxic cells due to hypoxia-induced chemoresistance (Fig. 5A and B). Besides, the nanocarrier CaO_2/MnO_2-MS showed minimal anti-proliferation effect against both normoxic and hypoxic SKOV3 cells. However, DOX delivered by the O_2-generating CaO_2/MnO_2-MS NPs showed significantly enhanced cytotoxicity towards hypoxic cells, indicating the hypoxia-relief and improved DOX chemotherapy. Notably, the cytotoxicity of DOX-CaO_2/MnO_2-MS NPs against L02 cells was largely reduced (Fig. 5C), possibly owing to the lower lipase activity in L02 cells which was not able to
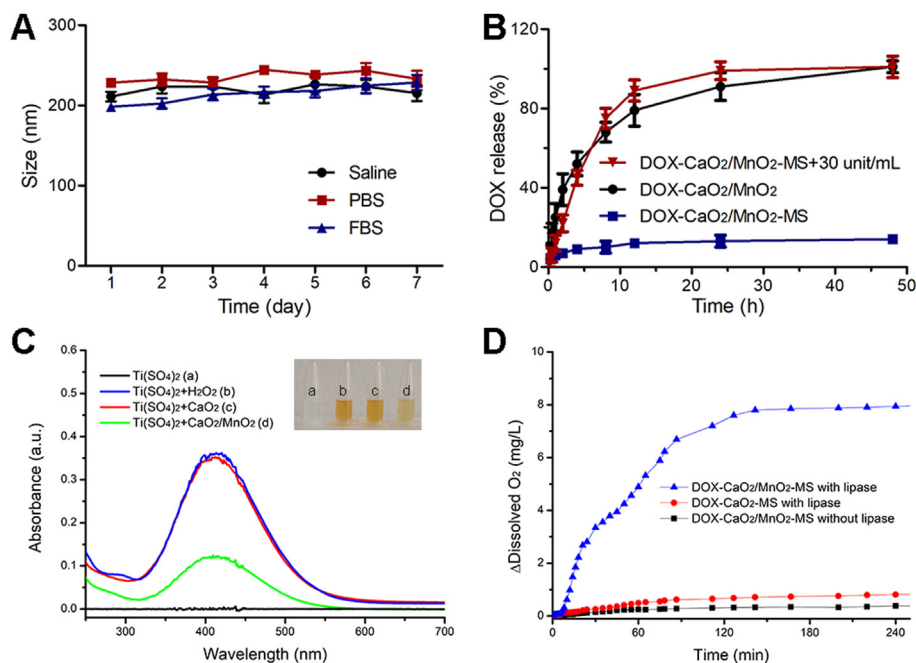
Figure 3 Stability and drug release of NPs. (A) Time-dependent colloidal stability of DOX-CaO$_2$/MnO$_2$-MS NPs in saline, PBS and FBS. Data are presented as mean $\pm$ SD, $n = 3$. (B) Lipase-triggered DOX release. Data are presented as mean $\pm$ SD, $n = 3$. (C) The H$_2$O$_2$-producing ability of CaO$_2$. (D) Lipase-triggered O$_2$ generation.

effectively trigger the free drug release as described in previous cell uptake analysis. In all, these results demonstrated that DOX-CaO$_2$/MnO$_2$-MS NPs could achieve enhanced chemotherapy towards hypoxic cancer cells with intratumoral lipase specificity.

To further explore the capacity of DOX-CaO$_2$/MnO$_2$-MS NPs to induce apoptosis, the Annexin V-APC/7-AAD method was used. As revealed by Fig. 5D and Supporting Information Fig. S3, the total percentage of apoptotic cells (including early and late apoptotic cells) induced by DOX-CaO$_2$/MnO$_2$-MS NPs reached 62.8% in hypoxic SKOV3 cells, far exceeding the findings in free DOX and the O$_2$-generating carrier groups (CaO$_2$/MnO$_2$-MS NPs), which demonstrated that the introduction of O$_2$ could

bolster chemotherapy-induced cell apoptosis. In accordance with the above MTT assay, the increased apoptosis by O$_2$ supply in normoxic cells was not that obvious as in hypoxic cells.

3.5. In vitro mechanism studies

In contrast to conventional free drugs and pH-responsive nanomedicines, our smart nanoformulation was expected to induce a neighboring effect by its lipase-triggered water-responsiveness, which contributed to an enhanced therapeutic outcome[31]. To valid our assumption, the intercellular trafficking of free DOX and NPs was studied in vitro. As the counterpart with water stability, MS-
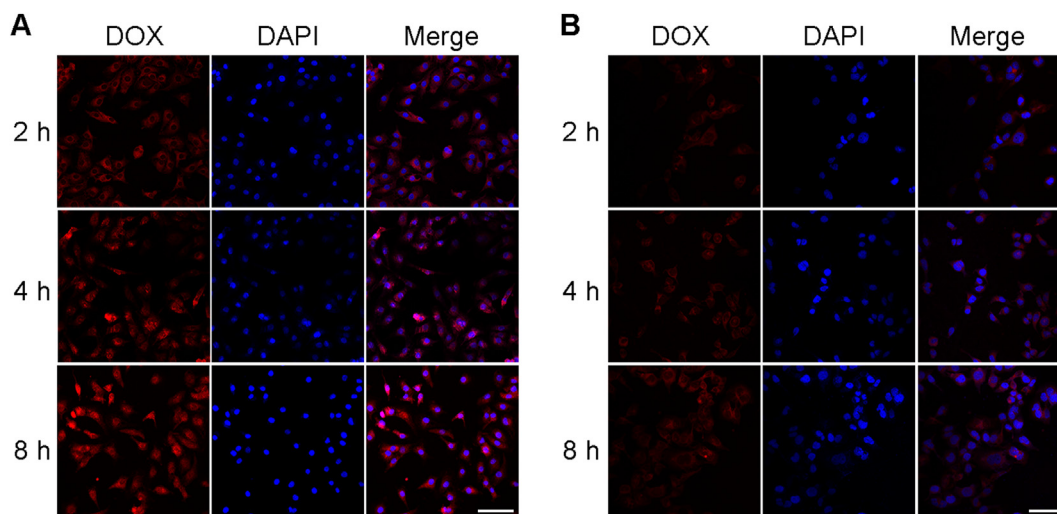

Figure 4 Cellular uptake of DOX-CaO$_2$/MnO$_2$-MS NPs in SKOV3 (A) and L02 (B) cells. Cell nuclei was stained with DAPI (blue fluorescence), DOX concentration: 1 μmol/L, scale bar = 200 μm.
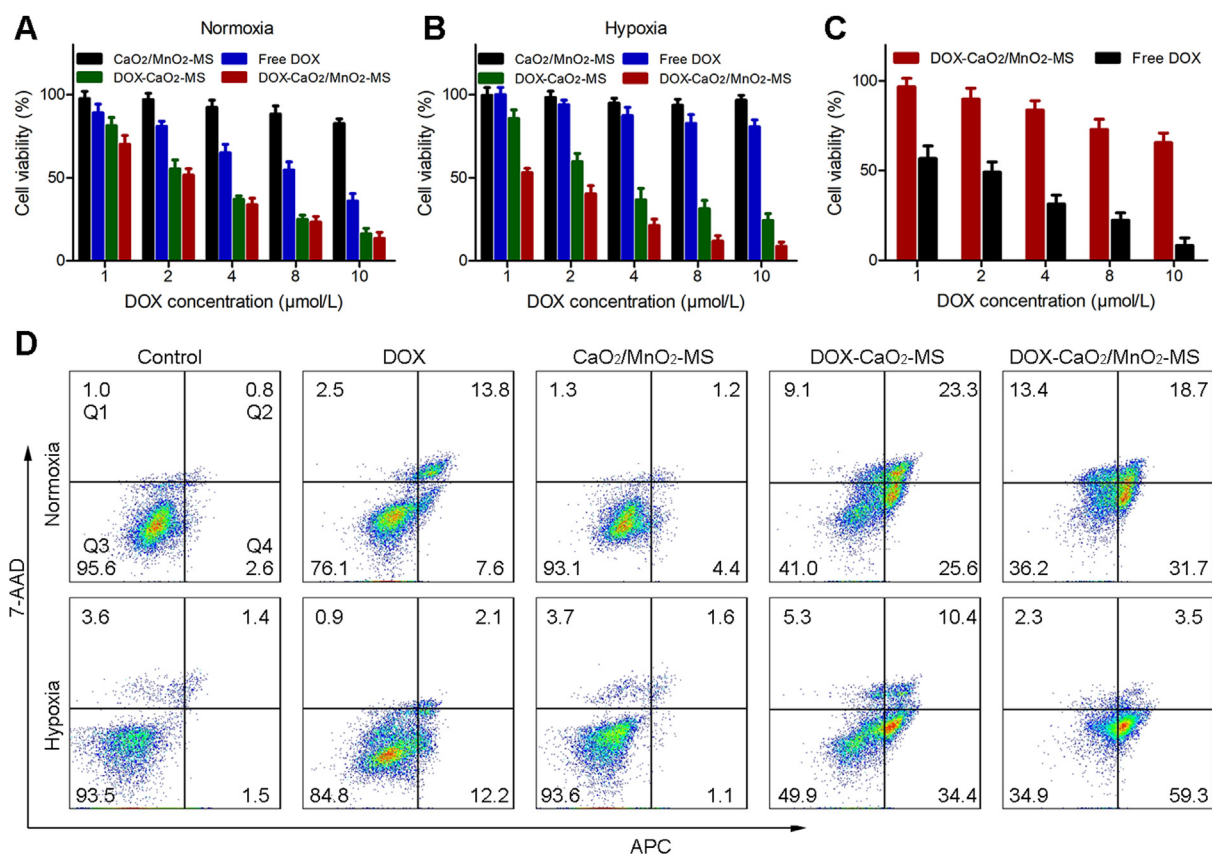
Figure 5 Selective and enhanced anticancer efficacy of NPs *in vitro*. Cell viabilities of SKOV3 cells after the treatments under normoxia (A) and hypoxia (B). (C) Cell viabilities of L02 and SKOV3 cells after the incubation with DOX-CaO$_2$/MnO$_2$-MS NPs. Data are presented as mean ± SD, n = 3. (D) The Annexin V-APC/7-AAD apoptosis assay of SKOV3 cells after the treatments under normoxia and hypoxia. DOX concentration: 4 μmol/L. Data are presented as mean ± SD, n = 3.

coated crystallized calcium carbonate (CaCO$_3$) was synthesized to load DOX in a similar method. First, the SKOV3 cells seeded on a coverslip were cultured with free DOX or NPs for 8 h. Then another coverslip with fresh cells was co-incubated with the treated cells (a) for another 24 h, which was repeated, followed by the observation using CLSM. As shown in Fig. 6A, successive cells (b) of DOX-CaO$_2$/MnO$_2$-MS NPs group revealed strong DOX fluorescence, and it was still detected in the third-generation cells (c). In contrast, the successive cells in free DOX group did not show obvious red fluorescence, possibly due to the strong interaction between DOX and DNA base-pairs which is responsible for entrapping DOX and depriving its ability to further infect neighboring cells. Interestingly, DOX-CaCO$_3$-MS NPs also showed minimal DOX signal in successive cells. It could be attributed to the phenomenon that the pH-dependent drug release of loaded DOX might be impeded by H$^+$ consumption. Thus, we can conclude that the lipase-triggered water-responsive DOX-CaO$_2$/MnO$_2$-MS NPs could achieve enhanced intercellular delivery of DOX, which could account for the improved chemotherapy.

We also performed an apoptosis assay to validate the neighboring effect. As displayed in Supporting Information Fig. S4, green fluorescence was weak in the groups of free DOX or DOX-CaCO$_3$-MS NPs, which indicated a smaller number of apoptotic cells. In comparison, DOX-CaO$_2$/MnO$_2$-MS NPs treated cells showed much stronger green fluorescence, suggesting that severer

cell apoptosis was induced by DOX-CaO$_2$/MnO$_2$-MS NPs-mediated neighboring effect.

The influence of DOX-CaO$_2$/MnO$_2$-MS NPs on the intracellular O$_2$ was tested using a commercial hypoxia probe, [Ru (dpp)$_3$]Cl$_2$. In the hypoxic condition, SKOV3 cells without treatments displayed the strongest red fluorescence, which indicated the lowest O$_2$ availability. After the cells were cultured with CaO$_2$/MnO$_2$-MS NPs for 12 h, the intracellular O$_2$ level increased significantly, but only slight O$_2$ production was detected in CaO$_2$-MS group treated cells (Fig. 6B). This could be ascribed to the strong catalytic ability of MnO$_2$ for O$_2$ generation.

It has been well-established that tumor hypoxia has an impact on the anti-tumor efficacy of chemotherapy by regulating HIF-1 pathways[32]. P-gp, which is closely related to DOX efflux and reduced chemotherapy efficacy, was demonstrated to be expressed in an HIF-1 dependent manner. Besides, CTGF regulated by HIF-1 acts as a critical regulator on collagen deposition in tumor tissue, which can impede drug penetration. Based on the hypoxia relief capacity of NPs, we speculated that the HIF-1 and its downstream proteins could be downregulated by the O$_2$-generating NPs. As expected, the results obtained by western blot analysis proved that the HIF-1α/P-gp and HIF-1α/CTGF/Collagen I pathways were largely inhibited by DOX-CaO$_2$/MnO$_2$-MS NPs. In accordance with the above determined O$_2$ generating ability, the MnO$_2$-free CaO$_2$ NPs could not suppress the HIF-1 pathways efficiently. Therefore, both drug penetration and drug retention could be
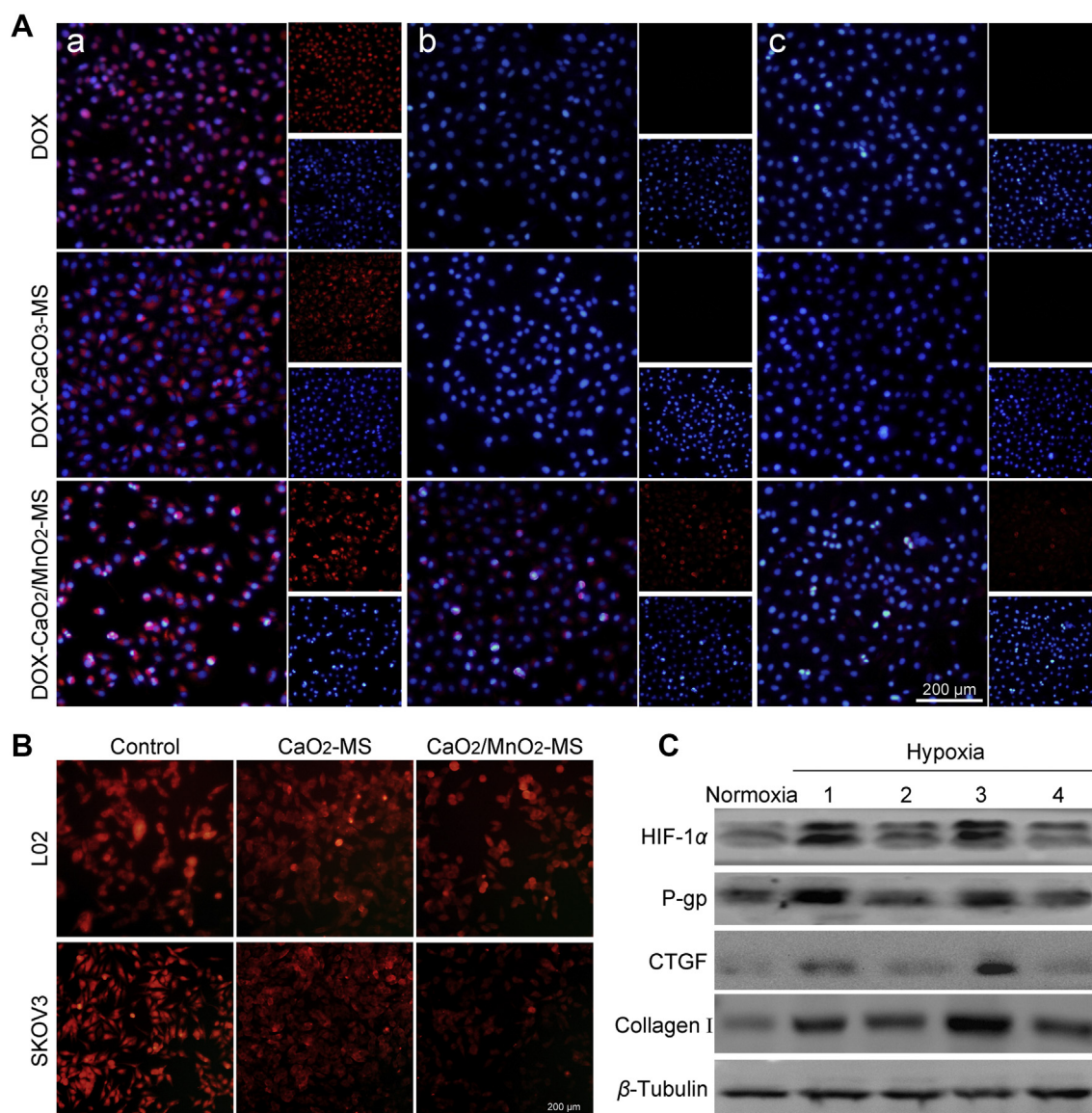
Figure 6 *In vitro* antitumor mechanisms. (A) Intercellular delivery of DOX from treated SKOV3 cells to fresh SKOV3 cells, cell nuclei was stained with DAPI (blue fluorescence), DOX concentration: 1 μmol/L, scale bar = 200 μm. (B) O_2 detection of hypoxic SKOV3 cells by [Ru $(dpp)_3]Cl_2$ probe, scale bar = 200 μm. (C) Immunoblot of endogenous HIF-1α and its downstream P-gp, CTGF, collagen I after different treatment (1) control; (2) CaO_2/MnO_2-MS; (3) DOX; (4) DOX-CaO_2/MnO_2-MS under hypoxia.

improved by NPs-facilitated O_2-induced HIF-1 pathways inhibition, which is an explanation for enhanced DOX chemotherapy.

3.6. Drug penetration and inhibition on MCTS

An SKOV3 MCTS model was constructed to evaluate the penetration capacity of DOX-CaO_2/MnO_2-MS NPs. As shown in Fig. 7A, DOX fluorescence only showed at the periphery of the tumor spheroids treated with DOX-$CaCO_3$-MS NPs. In contrast, DOX showed enhanced penetration in DOX-CaO_2-MS NPs treated MCTS. This phenomenon could be attributed to the strong penetration ability of free molecular DOX released from water-responsive CaO_2 matrix. Interestingly, the DOX fluorescence spread in the center of MCTS in free DOX and DOX-CaO_2/MnO_2-

MS NPs treated group, even at 120 μm from the surface to the middle. Hence, we can conclude that O_2 generation by CaO_2/MnO_2 and the smart convertible nanoformulation design synergistically enhanced drug penetration, respectively by collagen decomposition and free DOX-mediated neighboring effect. Further, the inhibition effect of DOX-CaO_2/MnO_2-MS NPs on MCTS growth was also examined. As shown in Fig. 7B and C, DOX-$CaCO_3$-MS NPs showed minimal effects may due to the insufficient drug release compared with free DOX. As expected, DOX-CaO_2/MnO_2-MS NPs had the best inhibitory effect on the growth of MCTS, indicating the promoted anticancer efficacy in MCTS level. This might be the consequence of comprehensive optimized drug transportation including drug release, penetration, and retention.
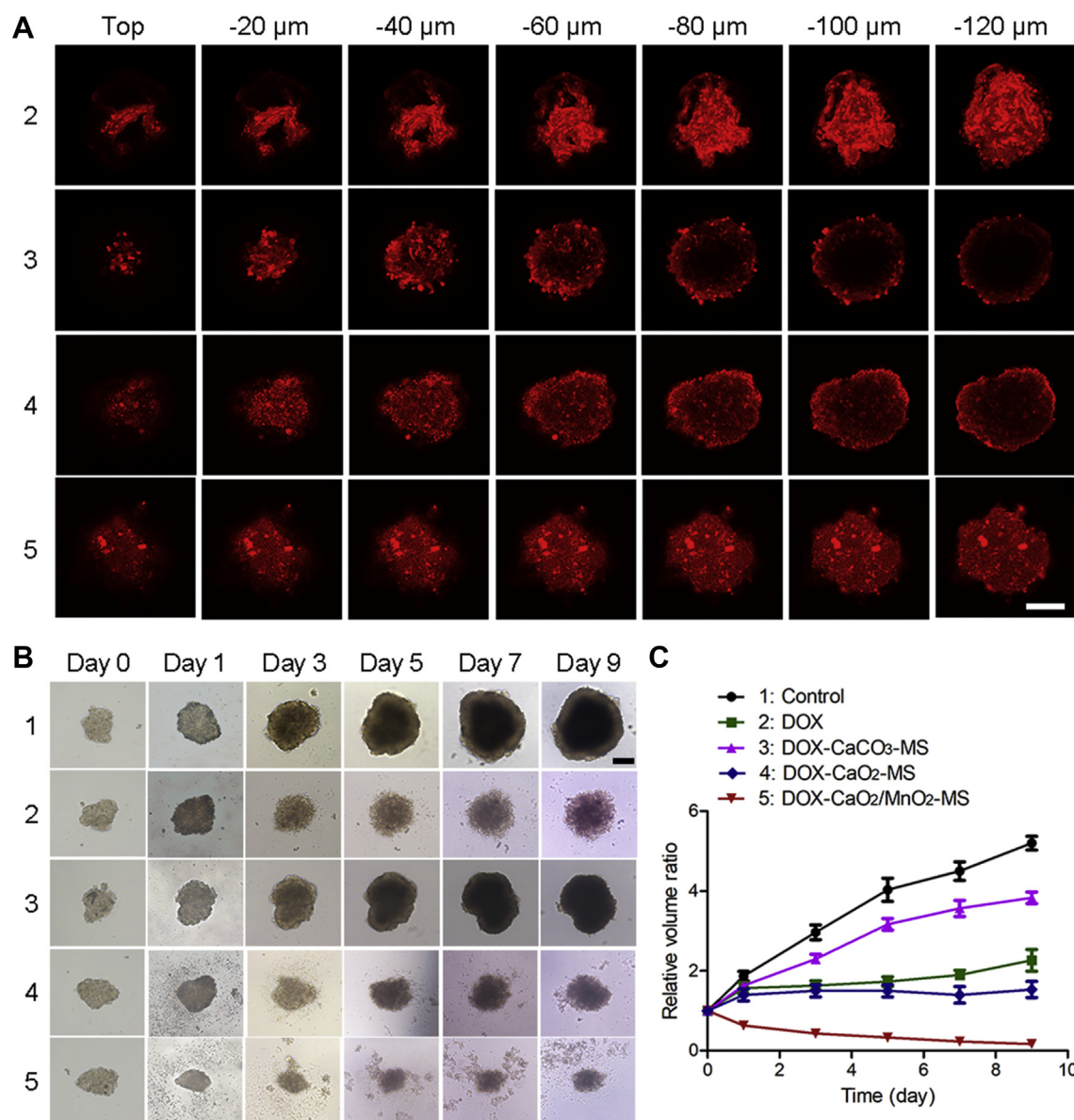
Figure 7 (A) *In vitro* penetration of DOX into the MCTS after incubation with different formulations for 24 h, DOX concentration: 2 μmol/L, scale bar = 200 μm. (B) MCTS inhibition effects, DOX concentration: 4 μmol/L, scale bar = 200 μm. (C) The volume change of MCTS. Data are presented as mean ± SD, $n = 5$.

3.7. Enhanced anticancer efficacy in vivo

SKOV3 cell xenograft model was employed to investigate the biodistribution and therapeutic efficacy of DOX-CaO_2/MnO_2-MS NPs *in vivo*. First, DiR as a near-infrared fluorescent probe was loaded into NPs to monitor the real-time *in vivo* distribution[33]. As displayed in Fig. 8A, free DiR was quickly metabolized, leading to a weak fluorescence detected in mice 48 h post-injection. However, at merely 4 h post-injection of NPs, the strong fluorescence was detected in the tumor tissue, confirming the preferable tumor-homing capability of NPs. This was also concluded by *ex vivo* fluorescence images obtained from mice after treatments with DOX-CaO_2/MnO_2-MS NPs (Supporting Information Fig. S5A) and free DOX (Fig. S5B) for 48 h.

To further explore the *in vivo* therapeutic efficacy of DOX-CaO_2/MnO_2-MS, NPs treatments started when the average tumor volume reached ∼150 mm³. As revealed in Fig. 8B−D, the DOX-CaO_2/MnO_2-MS NPs exhibited significantly enhanced tumor inhibition effect compared with CaO_2/MnO_2-MS NPs and free DOX, which proved the effectiveness of such smart O_2-generating nanocarrier in enhancing DOX chemotherapy *in vivo*. Moreover, no obvious weight loss was detected in all treated mice (Fig. 8E), indicating the biosafety of such solid lipid-based nanoformulation.

HIF-1α immunohistochemical analysis was further performed to measure the expression of HIF-1α protein. In line with the *in vitro* results, the HIF-1α signal was significantly downregulated in the O_2-generating groups (Fig. 9A), demonstrating the *in vivo* effect of hypoxia relief by NPs. As revealed using the TUNEL staining assay (Fig. 9B), intensive apoptosis was observed in tumor tissues after DOX-CaO_2/MnO_2-MS NPs treatment. And other therapeutic groups including free DOX and
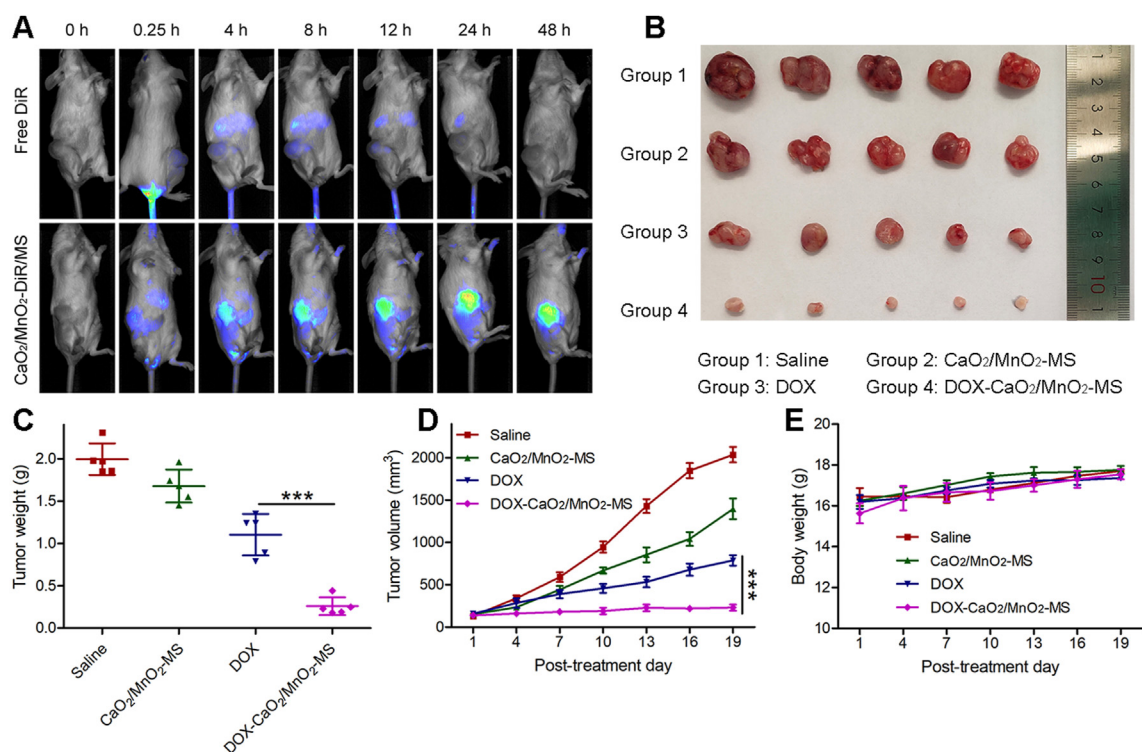
Figure 8 *In vivo* experiments. (A) Real-time fluorescence imaging of free DiR and CaO_2/MnO_2-DiR/MS NPs treated mice. (B) Tumor photographs, (C) average tumor weight, (D) tumor volume, and (E) average mouse body weight of saline and other treated groups. Data are presented as mean ± SD, $n = 5$, ***$P < 0.001$.
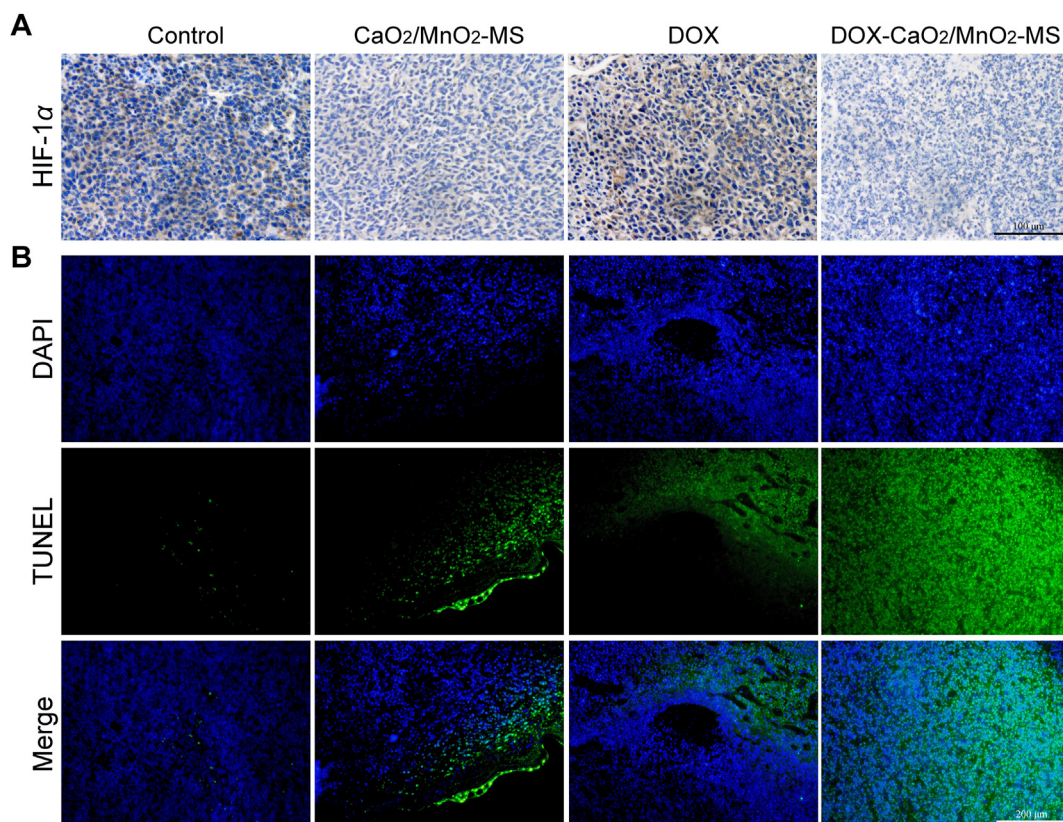

Figure 9 (A) HIF-1α staining images of the tumor, scale bar = 100 μm. (B) Representative images of tumor-site apoptosis determined by TUNEL assay, scale bar = 200 μm.

O$_2$-evolving nanocarrier didn't show such a strong effect. Finally, histological analyses of major normal organs including heart, liver, spleen, lungs, and kidneys confirmed the high biosafety with limited tissue damage in DOX-CaO$_2$/MnO$_2$-MS NPs-treated mice (Supporting Information Fig. S6).

4. Conclusions

In summary, a smart O$_2$-self-supplying nanocarrier was designed to enhance DOX chemotherapy by improving its transportation to cancer cells comprehensively. On one hand, the water-sensitive disintegration of drug-loaded CaO$_2$/MnO$_2$ cores not only enabled sufficient drug release, but also induced a neighboring effect with the assistance of MS coating, which potentiated drug penetration into deep tumor tissues. On the other hand, the generated O$_2$ downregulated HIF-1α and its downstream collagen I and P-gp, resulting in enhanced drug penetration and drug retention. Hence, the comprehensive optimized drug transportation including drug release, penetration, and retention was realized, which contribute to a better chemotherapeutic outcome.

Author contributions

Chuanchuan He, Xiaojuan Zhang, and Guangya Xiang designed the research. Xiaojuan Zhang carried out the experiments and performed data analysis. Yun Sun, Xiaoguang Liu, Yan Chen, Chen Chen, Ruicong Yan, and Ting Fan participated part of the experiments. Tan Yang, Yao Lu, Jun Luo, and Xiang Ma provided experimental drugs and quality control. Chuanchuan He and Xiaojuan Zhang wrote the manuscript. Jun Luo, Xiang Ma, and Guangya Xiang revised the manuscript. All of the authors have read and approved the final manuscript.

Conflicts of interest

The authors have no conflicts of interest to declare.

Appendix A. Supporting information

Supporting data to this article can be found online at https://doi.org/10.1016/j.apsb.2021.04.021.

References

1. Arruebo M, Vilaboa N, Sáez-Gutierrez B, Lambea J, Tres A, Valladares M, et al. Assessment of the evolution of cancer treatment therapies. *Cancers* 2011;**3**:3279−330.
2. Guo S, Miao L, Wang Y, Huang L. Unmodified drug used as a material to construct nanoparticles:Delivery of cisplatin for enhanced anticancer therapy. *J Control Release* 2014;**174**:137−42.
3. Browning RJ, Reardon PJT, Parhizkar M, Pedley RB, Edirisinghe M, Knowles JC, et al. Drug delivery strategies for platinum-based chemotherapy. *ACS Nano* 2017;**11**:8560−78.
4. Spencer DS, Puranik AS, Peppas NA. Intelligent nanoparticles for advanced drug delivery in cancer treatment. *Curr Opin Chem Eng* 2015;**7**:84−92.
5. Miao L, Guo S, Lin CM, Liu Q, Huang L. Nanoformulations for combination or cascade anticancer therapy. *Adv Drug Deliv Rev* 2017;**115**:3−22.
6. Minchinton AI, Tannock IF. Drug penetration in solid tumours. *Nat Rev Cancer* 2006;**6**:583−92.
7. Chen J, Ding J, Wang Y, Cheng J, Ji S, Zhuang X, et al. Sequentially responsive shell-stacked nanoparticles for deep penetration into solid tumors. *Adv Mater* 2017;**29**:1701170.
8. Ikeda Y, Hisano H, Nishikawa Y, Nagasaki Y. Targeting and treatment of tumor hypoxia by newly designed prodrug possessing high permeability in solid tumors. *Mol Pharm* 2016;**13**:2283−9.
9. Gilkes DM, Semenza GL, Wirtz D. Hypoxia and the extracellular matrix: drivers of tumour metastasis. *Nat Rev Cancer* 2014;**14**:430−9.
10. Fang Y, Sullivan R, Graham CH. Confluence-dependent resistance to doxorubicin in human MDA-MB-231 breast carcinoma cells requires hypoxia-inducible factor-1 activity. *Exp Cell Res* 2007;**313**:867−77.
11. Wu X, Zhu Y, Huang W, Li J, Zhang B, Li Z, et al. Hyperbaric oxygen potentiates Doxil antitumor efficacy by promoting tumor penetration and sensitizing cancer cells. *Adv Sci* 2018;**5**:1700859.
12. Huang CC, Chia WT, Chung MF, Lin KJ, Hsiao CW, Jin C, et al. An implantable depot that can generate oxygen *in situ* for overcoming hypoxia-induced resistance to anticancer drugs in chemotherapy. *J Am Chem Soc* 2016;**138**:5222−5.
13. Liu WL, Liu T, Zou MZ, Yu WY, Li CX, He ZY, et al. Aggressive man-made red blood cells for hypoxia-resistant photodynamic therapy. *Adv Mater* 2018;**30**:1802006.
14. Lan G, Ni K, Xu Z, Veroneau SS, Song Y, Lin W. Nanoscale metal-organic framework overcomes hypoxia for photodynamic therapy primed cancer immunotherapy. *J Am Chem Soc* 2018;**140**:5670−3.
15. Yu W, Shevtsov M, Chen X, Gao H. Advances in aggregatable nanoparticles for tumor-targeted drug delivery. *Chin Chem Lett* 2020;**31**:1366−74.
16. Yu W, Liu R, Zhou Y, Gao H. Size-tunable strategies for a tumor targeted drug delivery system. *ACS Cent Sci* 2020;**6**:100−16.
17. Cui T, Yan Z, Qin H, Sun Y, Ren J, Qu X. A sequential target-responsive nanocarrier with enhanced tumor penetration and neighboring effect *in vivo*. *Small* 2019;**15**:1903323.
18. Gong H, Chao Y, Xiang J, Han X, Song G, Feng L, et al. Hyaluronidase to enhance nanoparticle-based photodynamic tumor therapy. *Nano Lett* 2016;**16**:2512−21.
19. Ke CJ, Su TY, Chen HL, Liu HL, Chiang WL, Chu PC, et al. Smart multifunctional hollow microspheres for the quick release of drugs in intracellular lysosomal compartments. *Angew Chem Int Ed* 2011;**123**:8236−9.
20. Doublier S, Belisario DC, Polimeni M, Annaratone L, Riganti C, Allia E, et al. HIF-1 activation induces doxorubicin resistance in MCF7 3-D spheroids *via* P-glycoprotein expression: a potential model of the chemo-resistance of invasive micropapillary carcinoma of the breast. *BMC Cancer* 2012;**12**:4.
21. Wang C, Chen S, Wang Y, Liu X, Hu F, Sun J, et al. Lipase-triggered water-responsive "Pandora's Box" for cancer therapy: toward induced neighboring effect and enhanced drug penetration. *Adv Mater* 2018;**30**:1706407.
22. Zhang X, He C, Yan R, Chen Y, Zhao P, Li M, et al. HIF-1 dependent reversal of cisplatin resistance *via* anti-oxidative nano selenium for effective cancer therapy. *Chem Eng J* 2020;**380**:122540.
23. He C, Zhang X, Yan R, Zhao P, Chen Y, Li M, et al. Enhancement of cisplatin efficacy by lipid-CaO$_2$ nanocarrier-mediated comprehensive modulation of the tumor microenvironment. *Biomater Sci* 2019;**7**:4260−72.
24. He C, Zhang X, Chen C, Liu X, Chen Y, Yan R, et al. A solid lipid coated calcium peroxide nanocarrier enables combined cancer chemo/chemodynamic therapy with O$_2$/H$_2$O$_2$ self-sufficiency. *Acta Biomater* 2021;**122**:354−64.

25. Kwon HJ, Shin K, Soh M, Chang H, Kim J, Lee J, et al. Large-scale synthesis and medical applications of uniform-sized metal oxide nanoparticles. *Adv Mater* 2018;**30**:1−24.

26. Liu LH, Zhang YH, Qiu WX, Zhang L, Gao F, Li B, et al. Dual-stage light amplified photodynamic therapy against hypoxic tumor based on an O_2 self-sufficient nanoplatform. *Small* 2017;**13**:1701621.

27. Shen S, Mamat M, Zhang S, Cao J, Hood ZD, Figueroa-Cosme L, et al. Synthesis of CaO_2 nanocrystals and their spherical aggregates with uniform sizes for use as a biodegradable bacteriostatic agent. *Small* 2019;**15**:1902118.

28. Zhao Y, Luo Z, Li M, Qu Q, Ma X, Yu S, et al. A preloaded amorphous calcium carbonate/ doxorubicin@silica nanoreactor for pH-responsive delivery of an anticancer drug. *Angew Chem Int Ed* 2015;**3**:919−22.

29. Nomura DK, Long JZ, Niessen S, Hoover HS, Ng SW, Cravatt BF. Monoacylglycerol lipase regulates a fatty acid network that promotes cancer pathogenesis. *Cell* 2010;**140**:49−61.

30. He C, Zhang X, Xiang G. Nanoparticle facilitated delivery of peroxides for effective cancer treatments. *Biomater Sci* 2020;**8**:5574−82.

31. Guo S, Wang Y, Miao L, Xu Z, Lin CM, Zhang Y, et al. Lipid-coated cisplatin nanoparticles induce neighboring effect and exhibit enhanced anticancer efficacy. *ACS Nano* 2013;**7**:9896−904.

32. Onnis B, Rapisarda A, Melillo G. Development of HIF-1 inhibitors for cancer therapy. *J Cell Mol Med* 2009;**13**:2780−6.

33. Zhang X, He C, Liu X, Chen Y, Zhao P, Chen C, et al. One-pot synthesis of a microporous organosilica-coated cisplatin nanoplatform for HIF-1-targeted combination cancer therapy. *Theranostics* 2020;**10**:2918−29.